Rare Metal Materials and Engineering
Volume 55, Issue 2, February 2026
Available online at www.rmme.ac.cn

Science Press

Cite this article as: Zhao Cenya, Zheng Yang, Xiong Ruize, et al. Regulation of Microstructure, Mechanical Properties, and Corrosion Properties of Laser-Melting-Deposited B_4C/TC4 Composite by Heat Treatment[J]. Rare Metal Materials and Engineering, 2026, 55(02): 285-291. DOI: https://doi.org/10.12442/j.issn.1002-185X.20250051.

ARTICLE

Regulation of Microstructure, Mechanical Properties, and Corrosion Properties of Laser-Melting-Deposited B_4C/TC4 Composite by Heat Treatment

Zhao Cenya[1], Zheng Yang[1,2,5], Xiong Ruize[2], Ji Wenkang[2], Zhang Daohong[3], Liu Wei[4], Tao Hailin[5]

[1] School of Aeronautics and Astronautics, Tiangong University, Tianjin 300387, China; [2] School of Mechanical Engineering, Tiangong University, Tianjin 300387, China; [3] School of Environmental and Municipal Engineering, Tianjin Chengjian University, Tianjin 300384, China; [4] 3D Printing Research & Engineering Technology Center, AECC Beijing Institute of Aeronautical Materials, Beijing 100095, China; [5] Baoji Titanium Industry Co., Ltd, Baoji 721013, China

Abstract: The TiB+TiC dual-reinforced B_4C/TC4 composite was in-situ fabricated via incorporating 0.5wt% B_4C reinforcement during the laser melting deposition process. Different heat treatments of annealing and solid solution were used to regulate the microstructure, mechanical properties, and corrosion properties of B_4C/TC4 composite. Results show that with the increase in temperature from 500 °C to 800 °C, partial lamellar α-Ti in the as-deposited sample is gradually transformed into equiaxed α-Ti, accompanied by the disappearance of basketweave microstructure. At 1100 °C, a small portion of TiC phase suffers fusion. This composite exhibits the optimal combination of strength and plasticity after annealing at 500 °C for 4 h followed by furnace cooling, which is attributed to the stress release effect and the refined basketweave microstructure. However, this composite shows a decline in corrosion resistance after various heat treatments due to grain coarsening and micro-galvanic corrosion.

Key words: B_4C/TC4 composite; laser melting deposition; heat treatment; mechanical property; corrosion property

1 Introduction

TiB and TiC are common effective reinforcements in Ti-based composites. They are highly favored for their exceptional thermostability, excellent chemical compatibility with Ti, and thermal expansion coefficient close to that of Ti matrix[1]. As a result, the (TiB+TiC)/TC4 composite shows promising application prospects in the aerospace industry owing to its superior advantages in specific strength, wear resistance, and high-temperature stability[2]. Hu et al[3] investigated the microstructure and mechanical properties of (TiB+TiC)/TC4 composite fabricated by spark plasma sintering. The results showed that the size of both TiB and TiC was progressively increased with the increase in sintering temperature, resulting in an initial enhancement in strength and plasticity followed by a subsequent decline. Laser melting deposition (LMD), as an efficient additive manufacturing technique, shows great potential in fabricating high-performance Ti matrix composites (TMCs) [4]. Meng et al[5] employed LMD to prepare the (TiB+TiC)/TC4 composites by adding 1wt% – 5wt% nanosized B_4C. They found that the grains were refined from 600 μm to 11 μm in size with the increase in B_4C content, and the tensile strength reached 1310 MPa after adding 3wt% B_4C. Jiao et al[6] prepared the novel TC4-(TiB+TiC)/TC4 laminated composites by LMD and studied their microstructure evolution and microhardness changes after different annealing processes. The results demonstrated that the equiaxed level of these composites was improved and their microhardness values reached a maximum of 483.2 HV after annealing at 1000 °C.

Received date: February 23, 2025
Foundation item: Tianjin Municipal Natural Science Foundation (23JCYBJC00040); National Natural Science Foundation of China (52175369)
Corresponding author: Zheng Yang, Ph. D., Associate Professor, School of Aeronautics and Astronautics, Tiangong University, Tianjin 300387, P. R. China, E-mail: zhengyang@tiangong.edu.cn; Zhang Daohong, Ph. D., School of Environmental and Municipal Engineering, Tianjin Chengjian University, Tianjin 300384, P. R. China, E-mail: zhangdaohong@tcu.edu.cn

However, current research emphasis on the B_4C/TC4 composite has predominantly centered on their mechanical properties. The comprehensive regulations in the mechanical and corrosion properties of this composite through microstructure control via proper heat treatments are rarely reported. Consequently, in this research, the microstructure of LMD-B_4C/TC4 composite was tailored by two distinct kinds of heat treatment procedures (annealing and solid solution), and their influence on the resultant tensile and corrosion behavior was investigated to provide guidelines for the practical application of this composite.

2 Experiment

As shown in Fig. 1a and 1b, the spherical TC4 powders (99.5wt%) with a size range of 15–53 μm and the lamellate B_4C powders (0.5wt%) with size smaller than 50 μm were used as raw materials. A planetary ball mill (PM100, Retsch, Germany) was employed for the ball milling process. After adding the ball mill medium, argon gas was injected for 120 s and then vented for 20 s. The ball milling was conducted horizontally at 60 r/min and vertically at 300 r/min. The ratio of ball to material was 5∶1, and the powder was fully mixed for 10 h. The powder was ultrasonically cleaned with absolute ethyl alcohol, and the water and oxygen absorbed on the surface were removed by vacuum baking at 80 °C for 24 h. Fig. 1c depicts the schematic diagram of LMD process. The parameters of laser power, scanning speed, powder feeding rate, beam diameter, and *Z*-increment were set as 1200 W, 720 mm/min, 2.8 g/min, 2.0 mm, and 0.4 mm, respectively. In the molten pool, Ti and B_4C were in-situ reacted to generate the dual reinforcements of TiB and TiC under high-energy laser ($5Ti+B_4C \rightarrow 4TiB+TiC$). The thermal analysis experiment was performed in high-purity Ar atmosphere with heating and cooling rate of 10 °C/min, using a thermal analyzer (STA-449F5, Netzsch, Germany) to determine the appropriate heat treatment temperatures via analyzing the differential scanning calorimetry (DSC) and derived differential scanning calorimetry (DDSC) curves. Fig. 1d shows that DSC curve presents an obvious thermal effect peak at 805.4 and 1065.3 °C, corresponding to annealing temperature and phase change temperature, respectively. The cooling method of annealing was furnace cooling, and the cooling process of solid solution was water quenching. Based on Ref. [7], the detailed processing parameters of different heat treatments are shown in Fig.1e. The samples after treatments of LMD, LMD+annealing at 500 °C, LMD+annealing at 800 °C, and LMD+solid solution at 1100 °C were denoted as as-deposited, 500-annealing, 800-annealing, and 1100-solid solution ones, respectively. The samples for microstructure analysis and property evaluation were selected from the *X*-*Y* plane (perpendicular to the deposition direction). The microstructures (phase, morphology; fractured surface) were identified using X-ray diffractometer (XRD, D8 Advance, Bruker, Germany), backscattered electron diffractometer (EBSD, JSM-7900F, JEOL, Japan), and scanning electron microscope (SEM, JSM 6480, JEOL, Japan). The tensile behavior was tested at room temperature using a universal material testing machine (AGSX-50kND, SHIMADZU, Japan) with a strain rate of 1×10^{-3} s^{-1}. The corrosion behavior was evaluated in 3.5wt% NaCl solution at room temperature using an electrochemical workstation (LK2010, Tianjin Lanlike Chemical Electronic High-Tech Co., Ltd, China). The potentiodynamic polarization curves were recorded at the scan rate of 1 mV/s.

3 Results and Discussion

Fig.1f shows XRD patterns of different samples, presenting

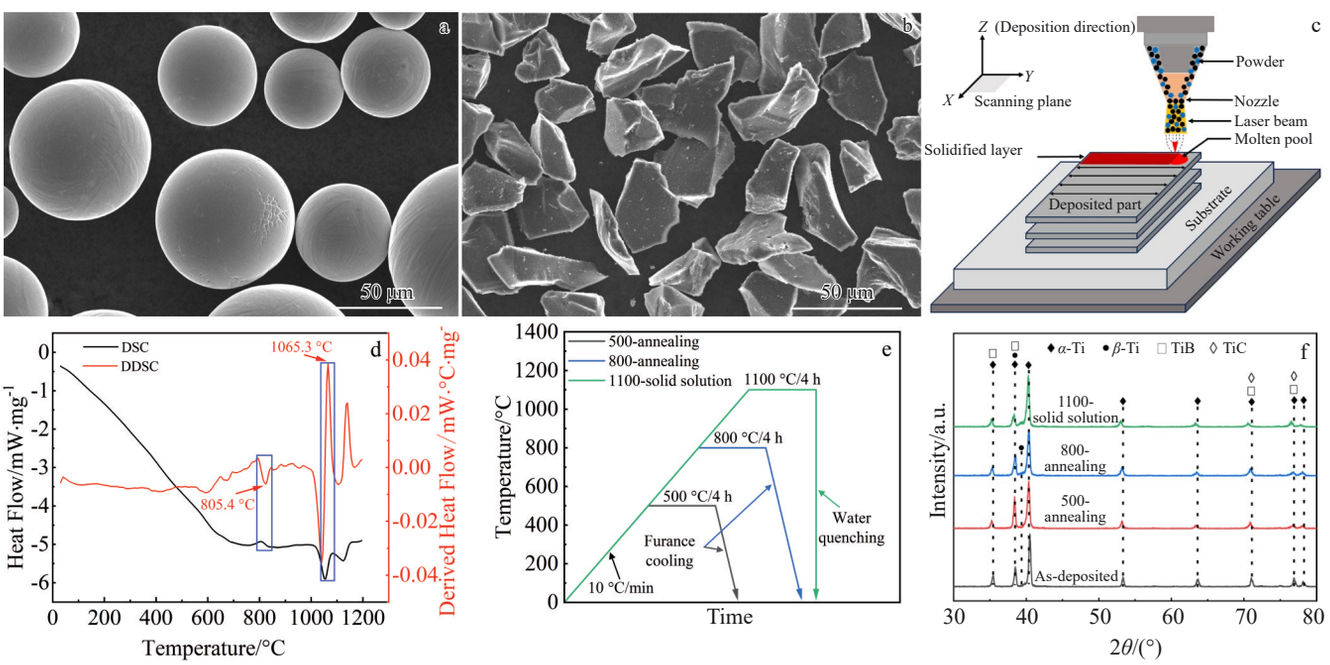

Fig.1 Morphologies of TC4 powder (a) and B_4C powder (b); schematic diagram of LMD process (c); DSC and DDSC curves of as-deposited sample (d); heat treatments of different samples (e); XRD patterns of different samples (f)

the phase components of the samples. The phase components of 500-annealing, 800-annealing, and 1100-solid solution samples remain consistent with those of the as-deposited sample, which are mainly composed of α-Ti (PDF 89-5009), β-Ti (PDF 89-3726), TiB (PDF 73-2148), and TiC (PDF 05-0693). No additional phases are generated, and no phases are decomposed, indicating the good thermal stability of this composite.

Fig. 2 shows the microstructures of different samples. As shown in Fig. 2a, the as-deposited sample exhibits a basketweave microstructure predominantly consisting of lamellar α-Ti surrounded by β-Ti. Different heat treatments result in varying degrees of microstructure evolution. For the 500-annealing sample (Fig. 2b), α-Ti preferentially nucleates along the grain boundaries of β-Ti at 500 °C, which leads to the decrease in size of lamellar α-Ti and the formation of finer basketweave microstructure[8]. For the 800-annealing sample (Fig. 2c), the nucleation and growth of α-Ti are more likely to occur. The original lamellar α-Ti is noticeably reduced and suffers spheroidization. On the one hand, high temperature can reduce the interfacial energy via dislocation annihilation, grain recovery, and recrystallization, which facilitates the spheroidization of lamellar α-Ti and the formation of equiaxed α-Ti[9]. On the other hand, high temperature contributes to the diffusion of element Al to stabilize the α-Ti, and the slow cooling process further promotes grain homogenization[10]. The elevated temperature accelerates the element diffusion process, reducing the diffusion anisotropy in α-Ti and thereby promoting its equalization[11]. Meanwhile, with the increase in temperature, the grain size is further increased, and the basketweave microstructure is disrupted, which is replaced by the bundled β-Ti[2,12–13]. For the 1100-solid solution sample (Fig. 2d), some TiC undergoes fusion and granulation at 1100 °C. As the temperature exceeds the phase transition point, the α-Ti is nearly converted into β-Ti, and a small amount of rod-shaped α-Ti exists in the layered β-Ti matrix. Similar phenomena can also be found in Ref.[2,14].

Fig. 3 shows a uniform distribution of elements B and C within the Ti matrix, indicating the uniform distribution of TiC and TiB phases.

Fig. 4a presents the tensile properties of different samples. The engineering stress-engineering strain curves and corresponding yield strength (YS), ultimate tensile strength (UTS), and elongation (EL) results are shown in Fig. 4b. The as-deposited sample has YS of 922.27±11.11 MPa, UTS of 985.09±16.22 MPa, and EL of 11.61%±1.54%. In contrast, the 500-annealing sample demonstrates slightly higher strength (YS=985.29±12.66 MPa; UTS=1068.35±11.77 MPa) and notably larger plasticity (EL=16.21%±1.69%), which is attributed to the stress release effect and the refined basketweave microstructure[15–17]. Firstly, the annealing treatment can facilitate atomic diffusion and dislocation rearrangement in some degree, thereby releasing the residual stress in the sample[18–19]. Secondly, the annealing treatment can cause the grains formed during the additive manufacturing to undergo polygonization through slip and climb, which results in the formation of sub-grain boundaries and leads to more uniform distribution of dislocations, reduced slip resistance, and enhanced deformation compatibility[20–21]. Thirdly, the annealing treatment can promote the activation of crystallographic slip system between adjacent grains to facilitate coordinated deformation of the lamellar α-Ti, thereby enhancing the ductility of the basketweave microstructure[11]. Furthermore, TiC and TiB are common reinforcing phases for the Ti matrix, since they have thermal expansion coefficient ($6.5\times10^{-6}-8.31\times10^{-6}$ K^{-1} for TiC; $8.3\times10^{-6}-8.50\times10^{-6}$ K^{-1} for TiB) similar to that of the Ti matrix ($8.2\times10^{-6}-8.6\times10^{-6}$ K^{-1})[22–23], which is beneficial to the strong

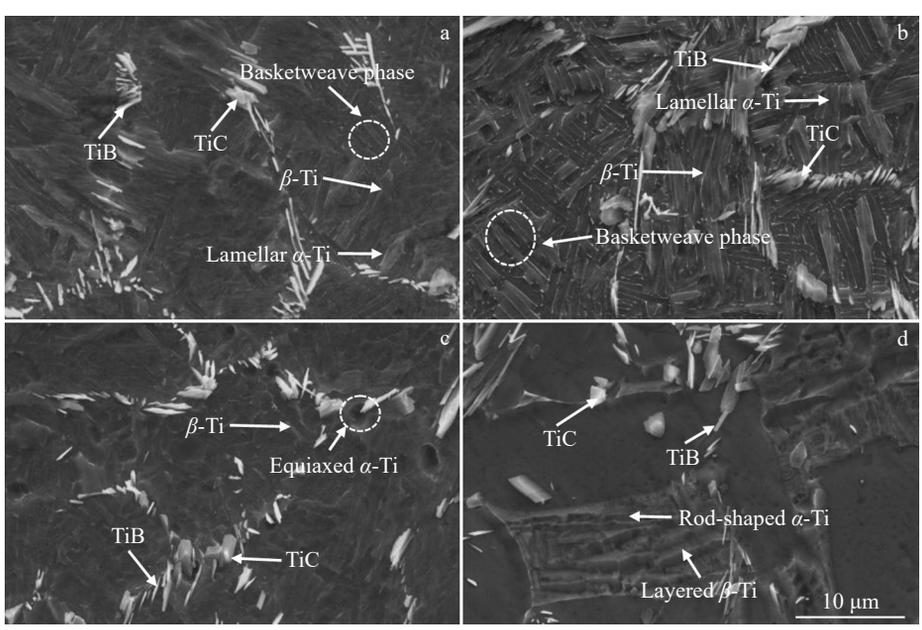

Fig.2 Microstructures of as-deposited (a), 500-annealing (b), 800-annealing (c), and 1100-solid solution (d) samples

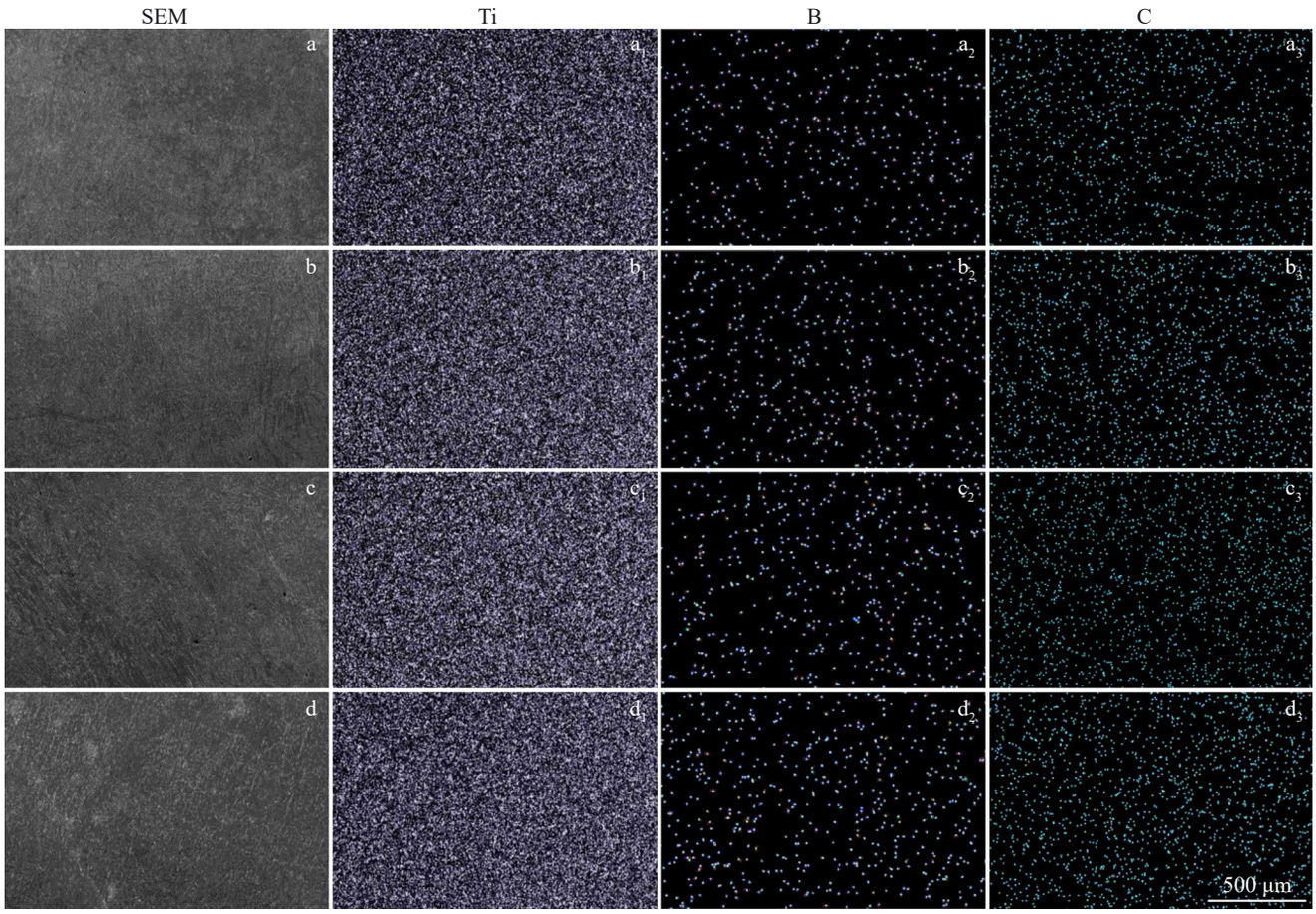

Fig.3 SEM images (a–d) and elemental distribution maps (a_1–a_3, b_1–b_3, c_1–c_3, d_1–d_3) of as-deposited (a, a_1–a_3), 500-annealing (b, b_1–b_3), 800-annealing (c, c_1–c_3), and 1100-solid solution (d, d_1–d_3) samples

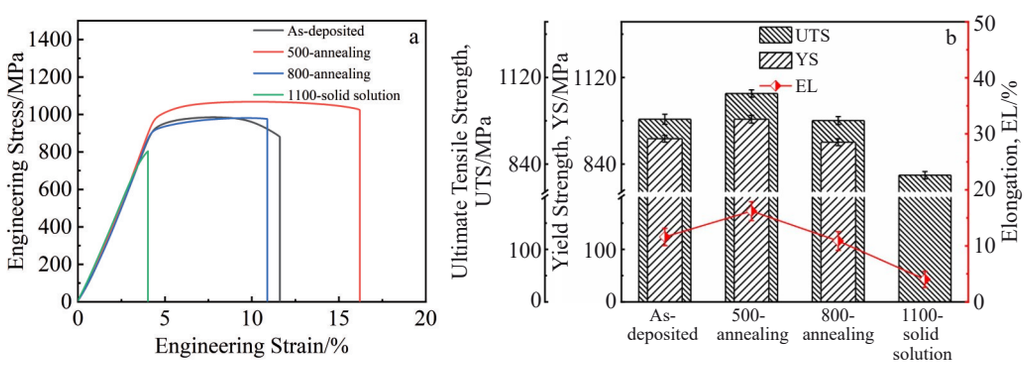

Fig.4 Tensile properties of different samples: (a) engineering stress-engineering strain curves; (b) YS, UTS, and EL results

interfacial interaction. The in-situ reaction between B_4C powders and TC4 powders during additive manufacturing contributes to the uniform distribution of TiC and TiB dual phases (Fig.3a–3d), which can enhance the Ti matrix via the synergetic effects of precipitation strengthening and dispersion strengthening[24–25]. Noticeably lower strength (YS=910.92±11.21 MPa; UTS=980.99±12.80 MPa) and smaller plasticity (EL=10.89%±1.67%), compared with those of the as-deposited sample, are found in the 800-annealing sample, which is owing to the coarsening of microstructures[26–27]. However, the 1100-solid solution sample suffers sudden fracture, showing inferior strength (UTS=804.55±11.80 MPa) and plasticity (EL=4.03%±1.43%) without any obvious yield phenomenon. This deterioration may be caused by the severe worsening of the microstructure, leading to the uneven distribution of the reinforcements[28]. The fracture surfaces of different samples are depicted in Fig.5. The fracture surface of the 500-annealing sample is similar to that of the as-deposited one, showing many dimples, which indicates a ductile fracture. Although the fracture surfaces of the 800-annealing sample still display dimple morphologies, the decrease in number of dimples signifies a decline in plasticity. However,

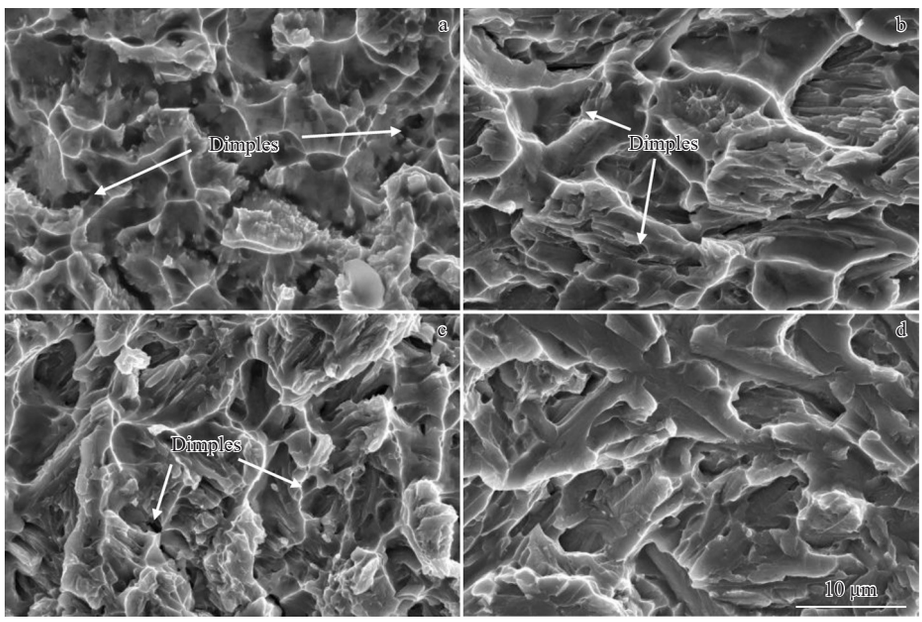

Fig.5 Fracture surfaces of as-deposited (a), 500-annealing (b), 800-annealing (c), and 1100-solid solution (d) samples

the fracture surface of the 1100-solid solution sample is distinguished by brittle feature. In summary, the 500-annealing sample possesses the optimal tensile properties, exhibiting the optimal combination of strength and plasticity.

Fig. 6 shows potentiodynamic polarization (PDP) curves of different samples. The corrosion potential (E_{corr}) and corrosion current density (i_{corr}) are fitted from PDP curves, and the results are listed in Table 1. A combination of higher E_{corr} and lower i_{corr} usually implies an enhanced corrosion resistance. The E_{corr} of the samples decreases in the order of as-deposited sample (−0.396 V vs. SCE)>500-annealing sample (−0.444 V vs. SCE)>800-annealing sample (−0.541 V vs. SCE)>1100-solid solution sample (−0.581 V vs. SCE). Conversely, the i_{corr} of the samples increases in the order of as-deposited sample (0.116 μA/cm^2)<500-annealing sample (0.289 μA/cm^2)<800-annealing sample (0.925 μA/cm^2)<1100-solid solution sample (5.063 μA/cm^2). The corrosion resistance of these samples undergoes varying degrees of deterioration after heat treatment, particularly when the samples are treated at elevated temperatures.

Fig. 7 shows grain structures and grain size results of different samples. It is proven that the β -Ti in the microstructure can somewhat enhance the corrosion resistance of Ti matrix[29]. The deterioration of corrosion resistance can be attributed to grain coarsening and micro-galvanic corrosion. For the grain coarsening part, the grains continuously

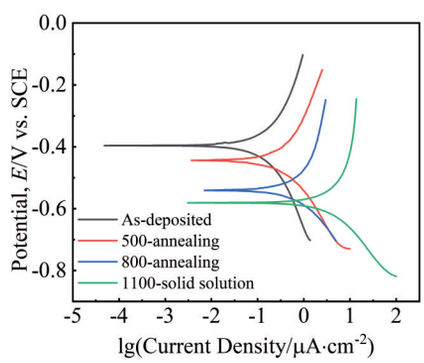

Fig.6 PDP curves of different samples

enlarge as the heat treatment temperature gradually increases. The average grain size of the as-deposited, 500-annealing, 800-annealing, and 1100-solid solution samples is 3.37, 4.13, 5.31, and 17.25 μm, respectively. The grain coarsening may eventually decrease the corrosion resistance via two main mechanisms. (1) Enhanced segregation of chemical composition within grains: grain coarsening often leads to an uneven distribution of alloying elements within the grains, which can accelerate localized non-uniform corrosion by promoting the formation of enhanced micro-galvanic cells[30]. (2) Decreased grain boundary density between grains: grain coarsening decreases grain boundary density, which impairs the formation, continuity, and stability of the passivation film, and

Table 1 Fitting results of corrosion potential (E_{corr}) and corrosion current density (i_{corr}) from Fig.6

Sample	Corrosion potential, E_{corr}/V vs. SCE	Corrosion current density, i_{corr}/μA·cm^{-2}
As-deposited	−0.396	0.116
500-annealing	−0.444	0.289
800-annealing	−0.541	0.925
1100-solid solution	−0.581	5.063

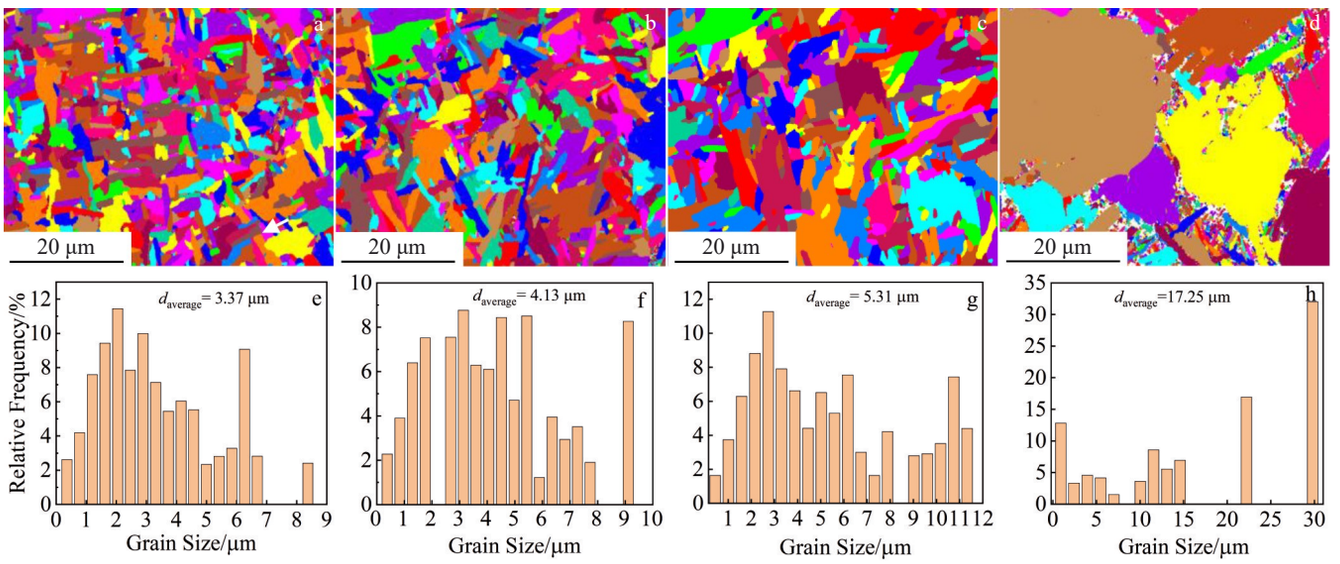

Fig.7 Grain sructures (a – d) and grain size results (e – h) of as-deposited (a, e), 500-annealing (b, f), 800-annealing (c, g), and 1100-solid solution (d, h) samples

hinders the development of a dense thick protective layer[31–32]. In addition, the decreased grain boundary density may damage the self-repair capacity of the passivation film, enabling corrosive attacks to propagate easily along straightforward grain boundary networks and thereby accelerating the corrosion process[33–34]. For the micro-galvanic corrosion part, the introduction of TiB and TiC may cause certain damage to the corrosion resistance of the material. The TiC and TiB are more inert than the Ti matrix[35]. Micro-galvanic corrosion occurs between the TiB/TiC reinforcement and the Ti matrix, where the TiB/TiC reinforcement with higher corrosion potential serves as the cathode to accelerate the dissolution of the Ti matrix and the Ti matric with lower corrosion potential acts as the anode[36–38].

Therefore, after heat treatment, the adverse effect of grain coarsening and micro-galvanic corrosion on corrosion resistance exceeds the beneficial effect of α-Ti/β-Ti transformation, ultimately deteriorating the corrosion resistance.

4 Conclusions

1) All the samples contain α-Ti, β-Ti, TiB, and TiC phases. The 500-annealing sample exhibits a microstructure comparable to that of the as-deposited sample, except for its refined lamellar α-Ti and basketweave structures. For the 800-annealing sample, its lamellar α -Ti is transformed into equiaxial α-Ti, and its basketweave structures no longer exist. For the 1100-solid solution sample, its α-Ti nearly converts into β-Ti, and some TiC undergoes fusion and granulation.

2) An optimal combination of mechanical and corrosion properties can be obtained for the LMD-prepared samples after annealing at 500 °C for 4 h followed by furnace cooling. The 500-annealing sample possesses the optimal strength (YS =985.29±12.66 MPa; UTS=1068.35±11.77 MPa) and plasticity (EL=16.21%±1.69%) due to the stress release effect and the refined basketweave microstructure. However, the 500-annealing sample displays slightly lower corrosion resistance due to the grain coarsening and micro-galvanic corrosion between the TiB/TiC reinforcement and the Ti matrix.

References

1 Jiang Botao, Wang Liang, Yan Hui *et al*. *Composites Communications*[J], 2023, 37: 101434
2 Zheng Bowen, Chen Shuai, Yue Chunyu *et al*. *China Foundry*[J], 2023, 20(3): 207
3 Hu Zhengyang, Peng Haichun, Zhang Zhaohui *et al*. *Materials Research Express*[J], 2021, 8(12): 126517
4 Zheng Yang, Xiong Ruize, Zhao Zihao *et al*. *Composites Communications*[J], 2024, 49: 101992
5 Meng Xin, Min Jin, Sun Zhonggang *et al*. *Composites Part B: Engineering*[J], 2021, 212: 108667
6 Jiao Tao, Jiang Tao, Dai Guoqing *et al*. *Materials Characterization*[J], 2023, 197: 112665
7 Huang Qingguo, Wang Zhilei, Feng Xinming *et al*. *Materials Science and Engineering A*[J], 2024, 912: 146987
8 Qi Chaoqi, Du Yang, Yang Ping *et al*. *Metals and Materials International*[J], 2022, 28(12): 3068
9 Sun Tao, Deng Yu, Liu Wenhao *et al*. *Journal of Alloys and Compounds*[J], 2024, 996: 174869
10 Wang Peng, Zhao Shuai, Nai Xin *et al*. *Materials Science and Engineering A*[J], 2024, 909: 146856
11 Liu Yingying, Tan Siyu, Yang Jian *et al*. *JOM*[J], 2024, 76(12): 6906
12 Yu Jiaxin, Yin Zhengpei, Huang Zhirong *et al*. *Materials*[J], 2022, 15(20): 7122
13 Zhao Yuantao, Yue Yongkang, Deng Wenlong *et al*. *Journal of Materials Research and Technology*[J], 2024, 33: 1155

14 Li Huizhao, Liang Kaiming, Pan Rui *et al*. *Rare Metal Materials and Engineering*[J], 2024, 53(5): 1287

15 Singla A K, Banerjee M, Sharma A *et al*. *Journal of Manufacturing Processes*[J], 2021, 64: 161

16 Zhu Yunlong, Zhao Qinglong, Ma Chunfeng *et al*. *Materials Science and Engineering A*[J], 2024, 912: 146998

17 Zheng Yang, Zhao Zihao, Liu Wei *et al*. *Journal of Mechanical Engineering*[J], 2024, 60(7): 385 (in Chinese)

18 Guo Xiongwei, Ren Zhongkai, Wu Han *et al*. *Journal of Iron and Steel Research International*[J], 2024, 23: 1

19 Xie Yong, Yan Zhenyu, Zhou Qingjun *et al*. *Additive Manufacturing Frontiers*[J], 2024, 3(4): 200168

20 Sun Junfeng, Lu Haifei, Liang Yuchen *et al*. *Materials Science and Engineering A*[J], 2024, 913: 147002

21 Prabhakaran B, Sivaraj P, Malarvizhi S *et al*. *Additive Manufacturing Frontiers*[J], 2024, 3(4): 200169

22 Ebrahimi A, Esfahani H, Fattah-Alhosseini A *et al*. *Journal of Materials Engineering and Performance*[J], 2019, 28: 1456

23 Du Liming. *Preparation and Research on Structure and Properties of (TiB+TiC)/Ti Composites*[D]. Harbin: Harbin Institute of Technology, 2010 (in Chinese)

24 Jiang Muchi, Ren Dechun, Cai Yushen *et al*. *Rare Metal Materials and Engineering*[J], 2022, 51(10): 3777 (in Chinese)

25 Zhang Wenjun, Yi Hao, Cao Huajun *et al*. *Chinese Journal of Rare Metals*[J], 2023, 47(5): 601 (in Chinese)

26 Zheng Yang, Xiong Ruize, Zhao Zihao *et al*. *Journal of Materials Engineering and Performance*[J], 2024, 34: 12410

27 Wang Cunyu, An Qi, Huang Lujun *et al*. *Composites Communications*[J], 2022, 36: 101357

28 Wu Tong, Yang Chunli. *The International Journal of Advanced Manufacturing Technology*[J], 2022, 121(9): 6303

29 Dai Nianwei, Zhang Laichang, Zhang Junxi *et al*. *Corrosion Science*[J], 2016, 111: 703

30 Wang Jincheng, Qin Peng, Liang Shunxing *et al*. *Materials Science and Engineering A*[J], 2019, 760: 214

31 Lu Wenqi, Wu Xiang, Liu Xiaochun *et al*. *Surface and Coatings Technology*[J], 2023, 470: 129849

32 Zheng Yang, Xiong Ruize, Zhao Zihao *et al*. *Journal of Materials Science & Technology*[J], 2025, 228: 137

33 Xu Weifeng, Zhang Wei, Wu Xiaoli. *Metallurgical and Materials Transactions A: Physical Metallurgy and Materials Science*[J], 2017, 48: 1078

34 Li Xuekai, Wang Wei, Wu Yihong *et al*. *Applied Surface Science*[J], 2024, 656: 159722

35 Han Jiaping, Gao Mengdie, Yu Yucheng *et al*. *Corrosion Science*[J], 2023, 215: 111013

36 Ding Yutian, Sun Fuhao, Xu Jiayu *et al*. *Chinese Journal of Rare Metals*[J], 2024, 48(5): 640 (in Chinese)

37 Zhao Yanchun, Zhang Minya, Zhang Linhao *et al*. *Rare Metal Materials and Engineering*[J], 2022, 51(11): 4146 (in Chinese)

38 Zheng Yang, Zhao Zihao, Xiong Ruize *et al*. *Progress in Natural Science: Materials International*[J], 2024, 34(1): 89

热处理对激光熔化沉积B_4C/TC4复合材料微观组织、力学性能及腐蚀性能的调控作用

赵岑芽[1]，郑　洋[1,2,5]，熊瑞泽[2]，冀文康[2]，张道虹[3]，刘　伟[4]，陶海林[5]

(1. 天津工业大学 航空航天学院，天津 300387)

(2. 天津工业大学 机械工程学院，天津 300387)

(3. 天津城建大学 环境与市政工程学院，天津 300384)

(4. 中国航发北京航空材料研究院 3D打印研究与工程技术中心，北京 100095)

(5. 宝鸡钛业股份有限公司，陕西 宝鸡 721013)

摘　要：在激光熔化沉积过程中加入0.5wt%的B_4C作为增强相，通过原位制备TiB+TiC双重增强TC4复合材料。通过固溶与退火2种不同热处理制度，对B_4C/TC4复合材料的微观结构、力学性能和腐蚀性能进行调控。结果表明：随着温度从500 ℃升高至800 ℃，沉积样品中的部分层状α-Ti逐渐转变为等轴状α-Ti，网篮组织也逐渐消失；在1100 ℃时，少量TiC相发生熔粒现象。复合材料在500 ℃退火4 h后炉冷的热处理制度下，强度和塑性的组合达到最佳状态，其性能提升主要归因于退火过程中产生的应力释放以及网篮组织的细化。然而，经各种热处理后，由于晶粒粗化和微电偶腐蚀的影响，复合材料的耐腐蚀性能有所下降。

关键词：B_4C/TC4复合材料；激光熔化沉积；热处理；力学性能；耐腐蚀性能

作者简介：赵岑芽，男，2001年，硕士生，天津工业大学航空航天学院，天津 300387，E-mail：zhaocenya@tiangong.edu.cn